



TECHNICAL ARTICLE

# Effect of Sealing Treatment on the Corrosion Resistance of Detonation-Sprayed Fe-Based Amorphous Coating

Haimin Zhai, Weichao Ning, Wensheng Li, Chunling Li, Jinfeng Jia, and Rongzhen Xiao

Submitted: 17 July 2022 / Revised: 21 October 2022 / Accepted: 23 November 2022 / Published online: 7 December 2022

Physical vapor deposition (PVD) was used to deposit a dense Cr film on the surface of Cr/Fe-based amorphous coating to seal the pores in detonation-sprayed Fe-based amorphous coatings and further improve the corrosion resistance of the Q235 steel substrate. The structure and corrosion behavior of the coating and film in 3.5 wt.% NaCl solution were investigated. Compared with Q235 carbon steel and Fe-based amorphous coatings, the Cr/Fe-based amorphous coating with Cr film deposited on the surface (coating) exhibited a lower corrosion current ( $2.2 \times 10^{-10}$  A) and corrosion rate ( $1.3 \times 10^{-4}$  mm/year), but a higher corrosion potential ( $-387$  mV) and polarization resistance ( $1.98 \times 10^5 \Omega \text{ cm}^2$ ). X-ray photoelectron spectroscopy (XPS) results show that  $\text{Cr}_2\text{O}_3$  and  $\text{Cr}(\text{OH})_3$  are abundantly present in the passivated film, improving the corrosion resistance of Cr/Fe-based amorphous coating and providing better protection to the Q235 steel substrate in 3.5 wt.% NaCl solution.

**Keywords** corrosion mechanism, detonation spraying, Fe-based amorphous coating, passivating film, PVD Cr film

## 1. Introduction

Because of their good corrosion resistance and wear resistance, Fe-based amorphous coatings (Fe-based ACs) provide corrosion and wear protection to metal substrate materials in extremely harsh environments (Ref 1-3). Over the past two decades, many thermal spraying techniques, such as high-velocity oxy-fuel (HVOF) spraying (Ref 4, 5), high-velocity air fuel (HVOF) spraying (Ref 6, 7), supersonic plasma spraying (Ref 8), and detonation spraying (Ref 9-11), have been used to prepare Fe-based ACs. Among these thermal spraying technologies, detonation spraying can be used to obtain dense and uniform Fe-based ACs (Ref 12-14). During the spraying process, acetylene and oxygen are detonated inside the chamber, then the powder is heated to a semi-melted state and accelerated to supersonic speed ( $\sim 400$  m/s) by the high-energy concentration detonation products at temperatures of up to 4500 K (Ref 13). The powder undergoes severe plastic

deformation to form flake particles when it impacts the substrate, resulting in a super strong bonding interface between the substrate and coating. Essentially, the powder is accelerated and heated by high-speed and hot detonation products flowing out of the barrel in pulsed mode with a typical frequency of 4 Hz, and the resultant substrate has a relatively low surface-working temperature of approximately 100 °C (Ref 15). For example, the amorphous phase content of detonation-sprayed FeCrMoCBY and FeCrBSiCMoCuNi ACs deposited on Q235 steel attained a maximum of 90.73% (Ref 11), which was higher than that of other deposition methods (69.33% for plasma spray (Ref 16), 81.25% for HVOF (Ref 17), and 74.9% for HVOF (Ref 18)).

Nevertheless, because the thermal spray coating is a layered structure formed by the deformation, interlacing, and accumulation of particles, thermal spray coating leads to the inevitable existence of many pores. Regardless of the optimization of several conditions, including the preparation process parameters, powder material morphology, and composition, pores inevitably form in thermal spray coating. The existence of pores affects the performance of the coating, especially in a corrosive environment, where the corrosive medium enters the coating through the pores and reaches the interface between the coating and substrate, inducing local corrosion and eventually causing coating failure. Zhang et al. used 3D high-resolution x-ray tomography (XRT) to study the porosity of Fe-based ACs and the effect of the size and distribution of pores on corrosion resistance. The penetration in the coating caused the anodic current to increase sharply, resulting in a decrease in the coating corrosion resistance, and penetration was effectively avoided only when the critical thickness of the AC exceeded 240  $\mu\text{m}$ . Therefore, avoiding the influence of pores on corrosion performance and maximizing the corrosion resistance of Fe-based ACs has become a bottleneck for industrial applications.

Recently, many attempts have been made to seal Fe-based ACs. Jiao et al. used an aluminum phosphate ( $\text{AlPO}_4$ ) sealant to seal HVOF-sprayed Fe-based ACs on a 304 stainless steel

Haimin Zhai, Wensheng Li, and Rongzhen Xiao, State Key Laboratory of Advanced Processing and Recycling of Non-Ferrous Metals, Lanzhou University of Technology, Lanzhou 730050, People's Republic of China; Weichao Ning, State Key Laboratory of Advanced Processing and Recycling of Non-Ferrous Metals, Lanzhou University of Technology, Lanzhou 730050, People's Republic of China; and Chongqing Hongjiang Machinery CO., LTD, Chongqing 402160, People's Republic of China; Chunling Li, School of Mechanical and Electrical Engineering, Lanzhou University of Technology, Lanzhou 730050, People's Republic of China; Jinfeng Jia, School of Materials and Chemical Engineering, Lanzhou College of Information Science and Technology, Lanzhou 730300, People's Republic of China. Contact e-mails: liws@lut.edu.cn and yxplcl@lut.edu.cn.

substrate and found that the aluminum phosphate sealant could penetrate into the coating and fill the microcracks, thereby significantly improving the corrosion resistance of the Fe-based ACs in HCl solution (Ref 19). Zhou et al. used a water-based silicone-modified acrylic sealant (WAS) with both sealing and anti-corrosion properties to seal Fe-based ACs. The water-based sealant improved the integrity of the passivated film of the coating. After soaking for 34 days, the corrosion current density of the sealing coating decreased by more than one order of magnitude, and the coating protection efficiency ( $\eta$ ) remained above 90% (Ref 20). Recently, our research group designed a composite duplex coating system of CrN/Cr<sub>3</sub>C<sub>2</sub>-NiCr (Ref 21) and DLC/Cr<sub>3</sub>C<sub>2</sub>-NiCr (Ref 22). The films were deposited on HVOF-sprayed Cr<sub>3</sub>C<sub>2</sub>-NiCr using physical vapor deposition (PVD), which not only realizes the sealing of the coating but also further improves the coating-wear resistance, corrosion resistance, and imparts high bearing resistance. The combination of thermal spraying and thin-film PVD or CVD can deposit a high-density, high-strength, high bonding film on the coating surface (Ref 23, 24), which can not only seal the surface of the coating but also protect the coating and the substrate by blocking the corrosive medium. However, the corrosion resistance of Fe-based ACs with sealing layers prepared by closed-field nonequilibrium magnetron sputtering has rarely been studied.

Herein, PVD was used to deposit Cr films on detonation-sprayed Fe-based ACs to seal pores, and the corrosion behavior of Fe-based AC and Fe-based AC with Cr films (Cr/Fe-based AC) was investigated in detail by characterization via dynamic polarization and electrochemical impedance spectroscopy (EIS) of the coatings in 3.5 wt.% NaCl solution. To evaluate the corrosion resistance of Fe-based AC and Cr/Fe-based AC, the microstructure and composition of the coatings before and after corrosion were characterized in detail using x-ray diffraction (XRD), scanning electron microscopy (SEM), and energy dispersive spectroscopy (EDS).

## 2. Experimental Details

### 2.1 Coating Preparation

The aerosolized commercial Fe-based amorphous powder (Guangzhou Wandun Co., Ltd, China) with a composition of approximately Cr 25-27, Mo 16-18, C 2.0-2.5, B 2.0-2.2, and Fe balance in wt.% was selected as the feedstock. Prior to spray, the Q235 steel substrate ( $\Phi 10 \times 10$  mm) was first subjected to grinding and acetone cleaning to remove surface oxide scale, oil, etc., followed by corundum sand blasting to increase the surface roughness of the substrate for the increased adhesion of thermal spray particles. Subsequently, the Fe-based AC was deposited on the clean and rough surface using a detonation spray system (ADM-4D), and the length and diameter of the barrel were 1000 and 25 mm, respectively. The charge in the gas mixture in the sprayed barrel was of approximately 60%. The powder feeder injected powder at 140 mm from the open end of the barrel, and the powder feed rate was 60 g min<sup>-1</sup>. Finally, using an unbalanced magnetron sputtering system (Teer UDP-650), a Cr thin film was deposited on the polished surface of the coating to seal the Fe-based AC surface. The detailed deposition parameters of the detonation spray (Ref 14) and PVD are listed in Tables 1 and 2, respectively.

### 2.2 Coating Characterization

XRD (D/Max-2400) was used to analyze the phase structure of the powder and coatings, and the scan rate and scan range were 2°/min and 20-90°, respectively. Field emission SEM (Quanta FEG 450) was used to characterize the microstructures of the powder and coatings and the corrosion morphologies of the coatings and Q235 substrate. Furthermore, EDS attached to the SEM was used to analyze the composition of the etched surface area of the coatings. A minimum of 15 SEM images of the polished surface at 200 × magnification were randomly selected to evaluate the average percentage of porosity using Image Pro-Plus 6.0. An electrochemical workstation (CHI760E) with a three-electrode system was used to evaluate the room-temperature corrosion behavior of the Fe-based AC, Cr/Fe-based AC, and Q235 steel substrates. The test samples were sealed with epoxy resin and exposed to a working electrode ( $\sim 10 \times 10$  mm). The electrochemical behavior was measured by open-circuit potential (OCP) for 1800s in 3.5 wt.% NaCl solution, AC impedance testing with an amplitude of 5 mV and frequency ranging from 0.01 to 10<sup>5</sup> Hz, and polarization curve testing with a scan rate of 0.01 V s<sup>-1</sup>. Zview software was used to analyze and fit the equivalent circuit model of the electrochemical impedance spectroscopy (EIS) results. After electrochemical testing, x-ray photoelectron spectroscopy (XPS, ESCALAB 250Xi) was used to analyze the elemental compositions and binding states of the Fe-based and Cr/Fe-based ACs.

## 3. Results and Discussion

### 3.1 Structural Characterization

Figure 1(a) presents the surface morphology of the Fe-based amorphous powder. Most of the powder is spherical or ellipsoid with a smooth surface; only a small portion of the morphology is spindle-like and thus is beneficial for detonation spraying. From the cross-sectional images in Fig. 1(b) and (d), the relatively dense Fe-based AC of approximately  $200 \pm 15$   $\mu$ m thickness, exhibiting good mechanical bonding with the substrate is observed. Additionally, according to the EDS composition analysis for the surface of the Fe-based AC in Fig. 2, the elemental distribution in the coating is relatively uniform. As observed from the unpolished surface image in Fig. 1(c), most of the particles melted well upon spraying, while the unmelted particles were fewer. This phenomenon was due to the acceleration and heating of the powder by the explosive products during detonation spraying. Owing to uniform heating, a completely molten powder was spread and deposited on the surface of the substrate. Additionally, sandblasting of the substrate also promoted good mechanical engagement of the powder particles with the substrate.

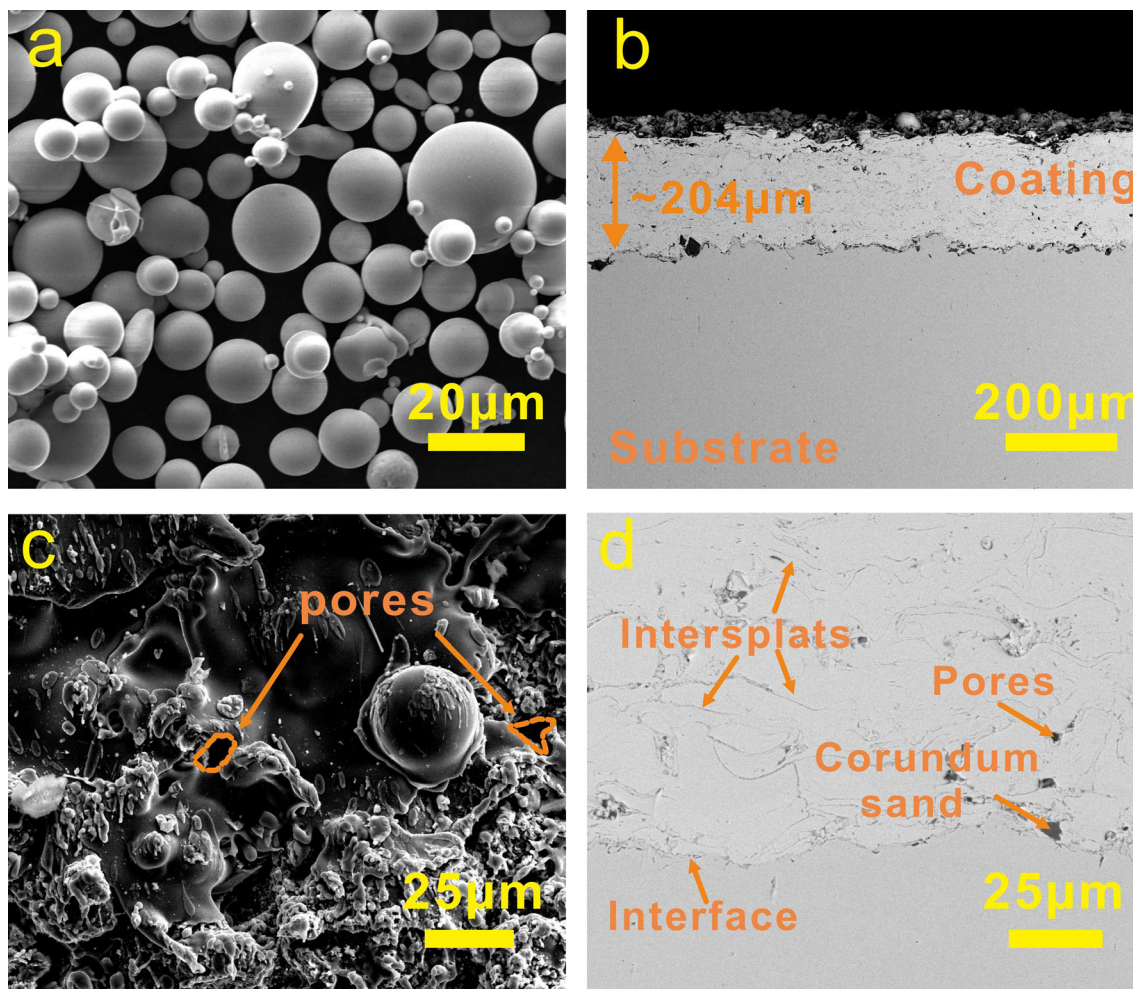
Figure 3(a) shows a cross-sectional image of the Cr/Fe-based AC. The Cr film, with an average thickness of approximately 3  $\mu$ m, not only has a very dense structure but also binds well to the Fe-based AC. The EDS line scanning composition distribution of the Cr/Fe-based AC in Fig. 2(b) shows that Fe, Cr, Mo, B, C, O, and other elements were continuously distributed, and only Cr was distributed in the film, indicating that the detonation-sprayed Fe-based AC was well combined with the PVD Cr film.

**Table 1 Detonation-sprayed parameters**

Working gas	Oxygen flow	Acetylene flow	Nitrogen flow	Working frequency	Spraying distance
O <sub>2</sub> + C <sub>2</sub> H <sub>2</sub>	0.5 m <sup>3</sup> h <sup>-1</sup>	0.25 m <sup>3</sup> h <sup>-1</sup>	0.05 m <sup>3</sup> h <sup>-1</sup>	3.9 Hz	140 mm

**Table 2 Deposition process parameters of Cr film**

Target current	Working pressure	Bias voltage	Deposition time	Deposition temperature
4 A	0.1 Pa	70 V	180 min	180 °C

**Fig. 1** (a) SEM image of the Fe-based amorphous powder, (b) cross-sectional morphology of Fe-based AC, (c) original morphology of Fe-based AC, (d) enlarge image of interface area between coating and substrate

The XRD patterns of the Fe-based amorphous powder, Fe-based AC, and Cr film in Fig. 4(a) show that the powder and coating exhibited typical amorphous diffused scattering peak patterns, indicating that the amorphous powder do not crystallize during detonation spraying. Correspondingly, single-phase Cr was observed in the XRD pattern of the film. Moreover, the EDS analysis results confirmed that the deposited film was a pure Cr film without other impurities (Fig. 4d). Using image

analysis software, it could be concluded that the porosity of the Fe-based AC was approximately 0.8%. Nevertheless, after passing through the PVD film, the surface of the film became dense and uniform, indicating that the pores were effectively sealed on the surface of the Fe-based AC.

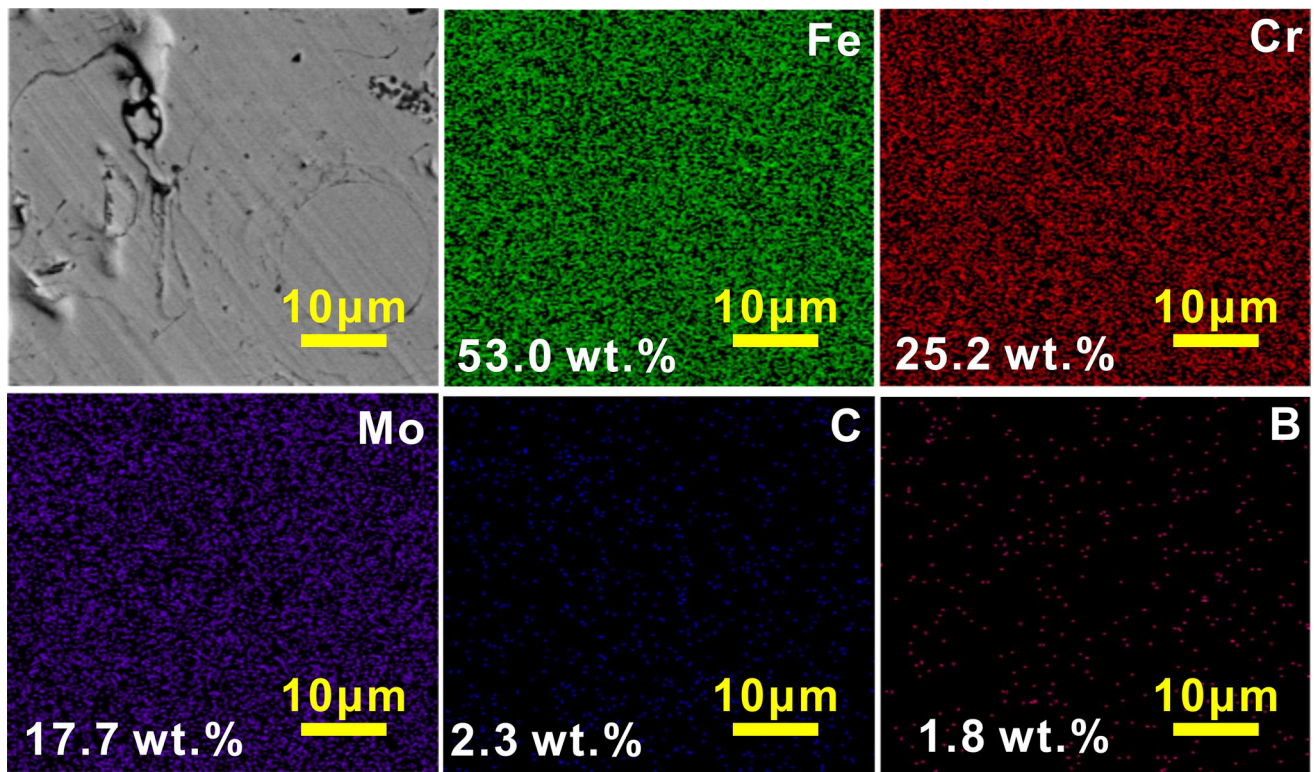


**Fig. 2** Results of EDS surface scanning composition and corresponding SEM photos of Fe-based amorphous coating

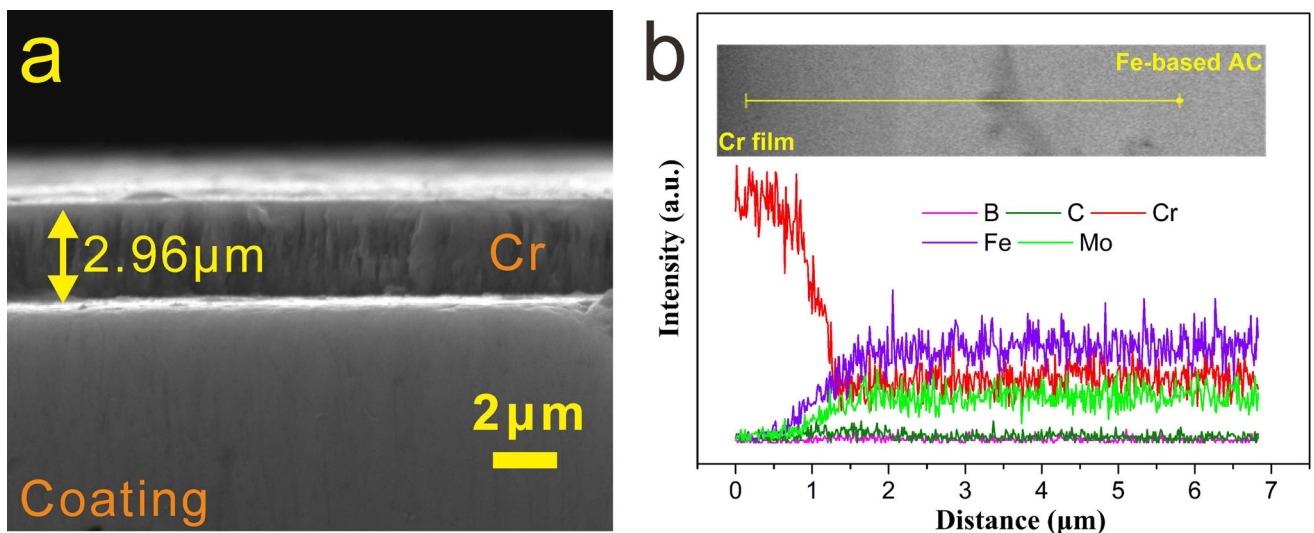


**Fig. 3** (a) cross section morphology of Cr/Fe-based AC, (b) the EDS element line scanning crossing the interfacial regions from Cr film to Fe-based AC

### 3.2 Corrosion Behavior in NaCl Solution

The corrosion behaviors of Q235 steel, Fe-based AC, and Cr/Fe-based AC were investigated in 3.5 wt.% NaCl solution. Figure 5(a) shows the OCP results. Both the Fe-based and Cr/Fe-based ACs present a nearly positive potential, while the potential value of Q235 steel stabilized to  $-392.1$  mV after 1800s. However, for Fe-based AC, the potential decreased slightly as  $\text{Cl}^-$  in the solution penetrated the pores at the beginning of the experiment. Subsequently, a dense film was formed on the surface; thus, the potential value stabilized at

$-259.8$  mV. For the Cr/Fe-based AC, the OCP value slowly approached 0 mV within 0–400 s, indicating that in the early stage of the electrochemical experiment, the NaCl solution did not easily penetrate the film, and the entire system was not easily corroded. However, over time, the NaCl solution slowly infiltrated, causing the potential to decrease slowly and stabilize at  $-197.4$  mV. Moreover, compared with Q235 steel and the Fe-based AC, the Cr/Fe-based AC exhibited a relatively positive corrosion potential ( $-387$  mV) and a lower corrosion current density ( $-2.2 \times 10^{-10}$  A  $\text{cm}^{-2}$ ), indicating that the

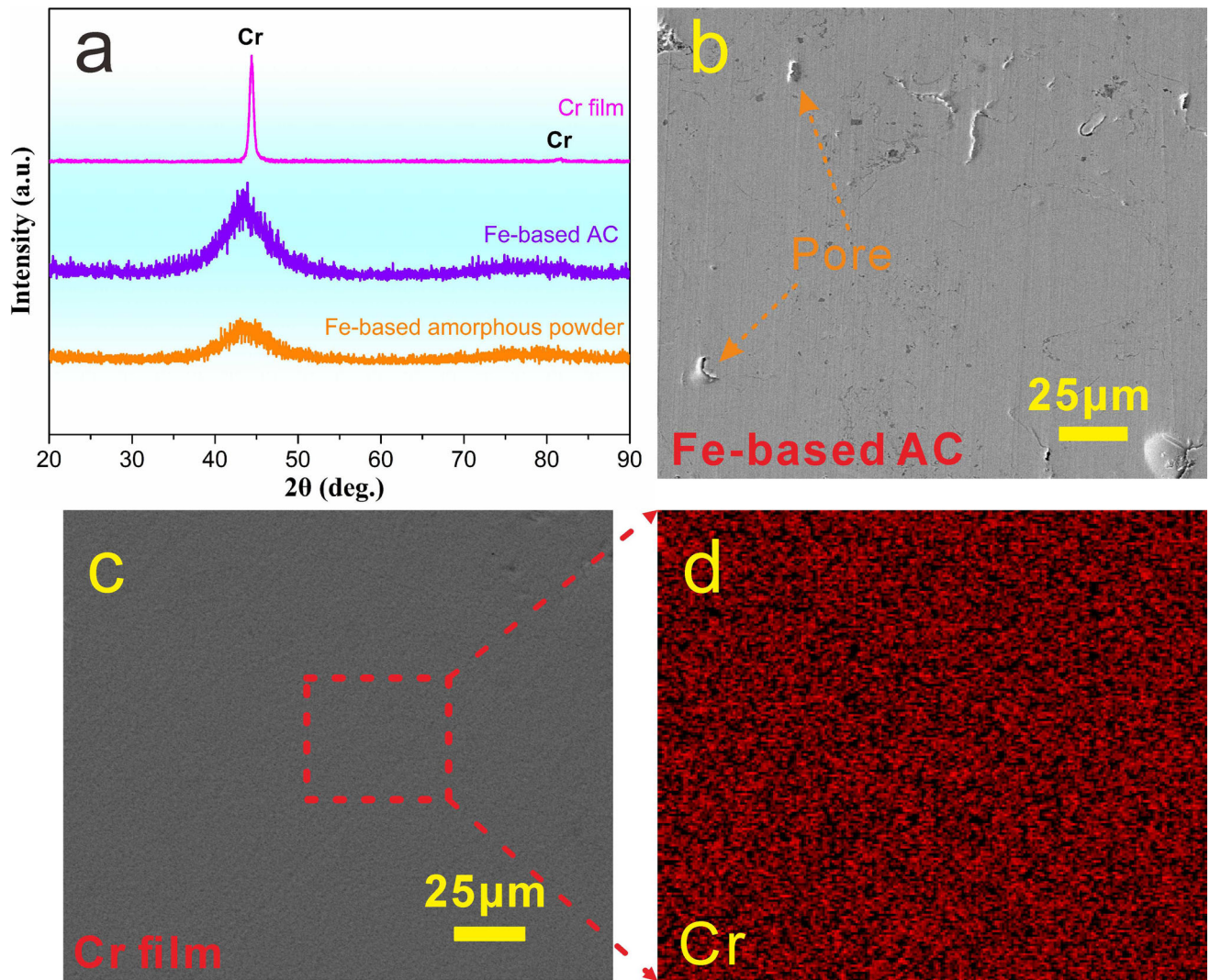


**Fig. 4** (a) XRD patterns of Fe-based amorphous powder, Fe-based AC and Cr film, (b) the morphology of Fe-based AC, (c) the morphology of Cr/Fe-based AC, (d) the EDS surface scan of Cr film surface

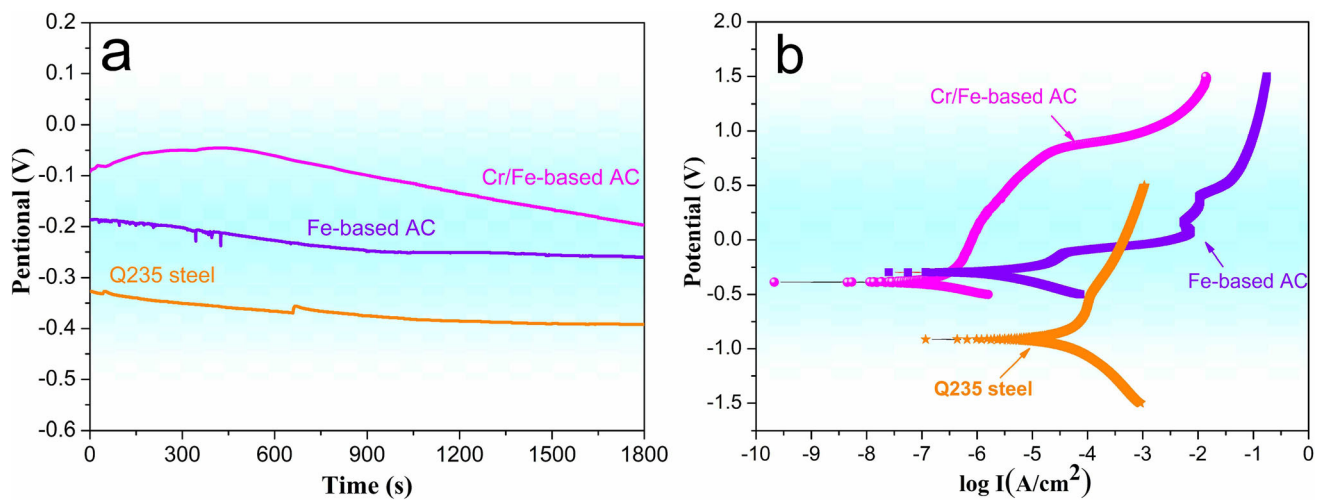


**Fig. 5** Electrochemical performance test results of Q235 steel, Fe-based AC, and Cr/Fe-based AC in 3.5 wt.% NaCl solution: (a) open-circuit potential, (b) polarization curve

corrosion resistance of the Cr/Fe-based AC was significantly improved.

Figure 6 shows the Nyquist plots of Q235 steel, Fe-based AC, and Cr/Fe-based AC. The diameter of the semicircle represents the capacitive reactance arc, which is related to the polarization resistance of the working electrode (Ref 3). From Fig. 5(a), compared with Q235 steel, Fe-based, and Cr/Fe-based ACs have larger capacitive reactance arcs, indicating that the Cr/Fe-based AC possesses superior corrosion resistance. Particularly, the capacitive resistance value of Cr/Fe-based AC attained  $3.051 \times 10^5 \text{ } (\Omega \text{ cm}^2)$ , indicating that the deposition of Cr film by PVD assuages the problem of pores on the surface of thermally sprayed coatings. Moreover, due to the synergistic effect of the Cr film and Fe-based AC to block and shield  $\text{Cl}^-$  in NaCl solution, the Q235 steel substrate showed improved corrosion resistance.

Figure 6(b) shows the Bode plots of Q235 steel, Fe-based AC, and Cr/Fe-based AC. The Cr/Fe-based AC has the highest impedance ( $4.8 \times 10^5 \text{ } \Omega \text{ cm}^2$ ) value compared to those of Fe-based AC ( $1.3 \times 10^4 \text{ } \Omega \text{ cm}^2$ ) and Q235 steel ( $4.4 \times 10^3 \text{ } \Omega \text{ cm}^2$ ), indicating that the composite Cr/Fe-based AC system can effectively protect Q235 steel from the corrosive environment. Moreover, one peak (one single time constant) is observed at  $10^0$ - $10^2$  Hz for the Cr/Fe-based AC and Q235 steel, while two peaks (two single time constants) are observed for Fe-based AC (Fig. 6b). The changes in the impedance and capacitive reactance observed via the Bode plots (in the high-frequency area) are generally due to local unevenness and defects that often cause corrosion on the surface of the film and coating, while the middle- and low-frequency areas correspond to the film interface and the interface of coating and substrate, respectively (Ref 3, 18). In the intermediate frequency region ( $10^0$ - $10^2$  Hz), all phase angles tend to  $90^\circ$  for the Q235 steel, Fe-based AC, and Cr/Fe-based AC. Particularly, the phase angle of Cr/Fe-based AC attains  $80.5^\circ$ , which proves that the composite system in this state is similar to an infinite resistance capacitor without current, that is, the corrosive medium cannot continue to act on the composite system. In the high-frequency region ( $10^3$ - $10^5$  Hz), the phase angle tends to  $0^\circ$ , indicating the existence of charge-transfer resistance and film capacitance in Cr/Fe-based AC. Moreover, in the range of  $\sim 10^2$ - $10^5$  Hz, the phase angle of Cr/Fe-based AC shows a decreasing trend, which indicates that the capacitance value increased and the resistance value decreased. The trend also indicates that the corrosion medium  $\text{Cl}^-$  would slowly penetrate the Cr film, thereby changing the resistance and capacitance of the composite system, but the composite system would still protect the

Q235 steel substrate. Notably, in the low-frequency region ( $\sim 10^{-2}$ -1 Hz), the phase angle of the Cr/Fe-based AC is greater than that of Fe-based AC and Q235 steel, indicating that the composite system has better corrosion resistance.

Based on the above analysis, the electrochemical impedance spectroscopy (EIS) fitted results are used to display the electrochemical reaction of Q235 steel, Fe-based AC, and Cr/Fe-based AC, as presented in Fig. 7, where  $R_s$  is the resistance of NaCl solution,  $R$  is the charge-transfer resistance of the Q235 steel,  $\text{CPE}_{p0}$  is the constant phase-angle element corresponding to the Q235 steel,  $R_p$  is the resistance of the passivated film,  $R_c$  is the resistance of the Fe-based AC,  $\text{CPE}_{p0}$  is the constant phase element corresponding to the Q235 steel,  $C_c$  is the capacitance corresponding to the Q235 steel (between pore and coating) (Ref 25),  $R_f$  is the resistance at the interface between the Cr film and Fe-based AC,  $\text{CPE}_{p0}$  is the corresponding constant phase element formed with the passivated film and coating, which describes the non-ideal state of the electrode surface (Ref 26, 27),  $R_p$  is the resistance of the passivated film, and  $C_f$  is the capacitance formed at the interface between the Cr film and coating. From the EIS fitted results (Table 3), the resistance values of the Cr/Fe-based AC ( $R_f = 6.8 \times 10^5 \text{ } \Omega \text{ cm}^2$ ) are one order of magnitude higher than that of the Fe-based AC ( $R_c = 1.9 \times 10^4 \text{ } \Omega \text{ cm}^2$ ).

Figure 8 shows the corrosion morphology and corresponding composition distribution of the Cr/Fe-based AC. Local pitting occurs on the surface of the Cr/Fe-based AC. Figure 8(b), (c), (d), and (e) shows the enlarged topography and composition distribution of the corrosion pit after electrochemical corrosion for 1 h in a 3.5% NaCl solution, and the results show that Cr (94.7 wt.%), O (5.2 wt.%), Cl (0.1 wt.%), and other elements are distributed on the surface of the Cr/Fe-based AC after corrosion. The elements that comprise the Fe-based AC, such as Fe and Mo, were not observed, indicating that the Cr film effectively defended against  $\text{Cl}^-$  corrosion. Contrastingly, Fig. 9 shows the corrosion morphology and corresponding composition distribution of Fe-based AC. There is a slight segregation and oxidation of elements in the interfacial region of the Fe-based AC, leading to galvanic corrosion; thus, a large area is continuously corroded. Additionally, owing to continuous corrosion, the passivation film is gradually consumed, significantly reducing the Mo content in the corrosion pit.

### 3.3 Corrosion Mechanism

Usually, for an ideal amorphous coating in an ideal corrosive environment, a passivated film with uniform thickness is

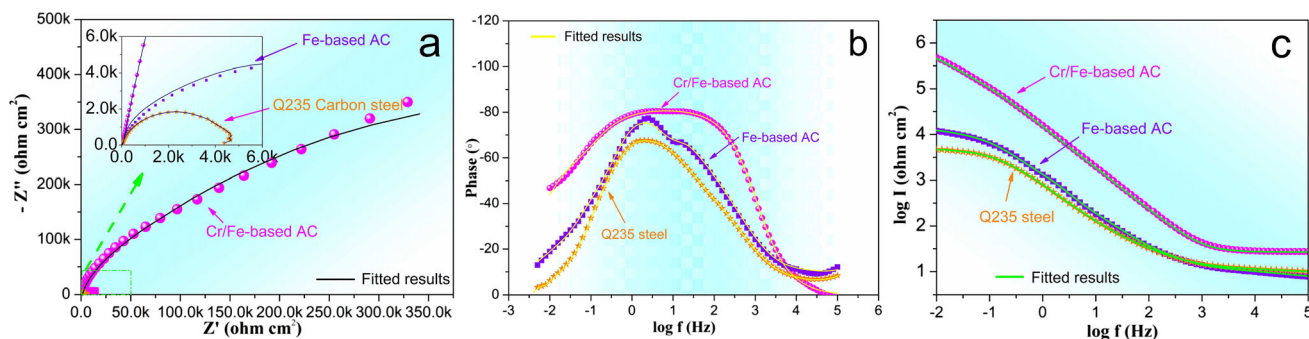


**Fig. 6** Electrochemical performance test results of Q235 steel, Fe-based AC, and Cr/Fe-based AC in 3.5 wt.% NaCl solution: (a) Nyquist plots; (b, c) Bode plots

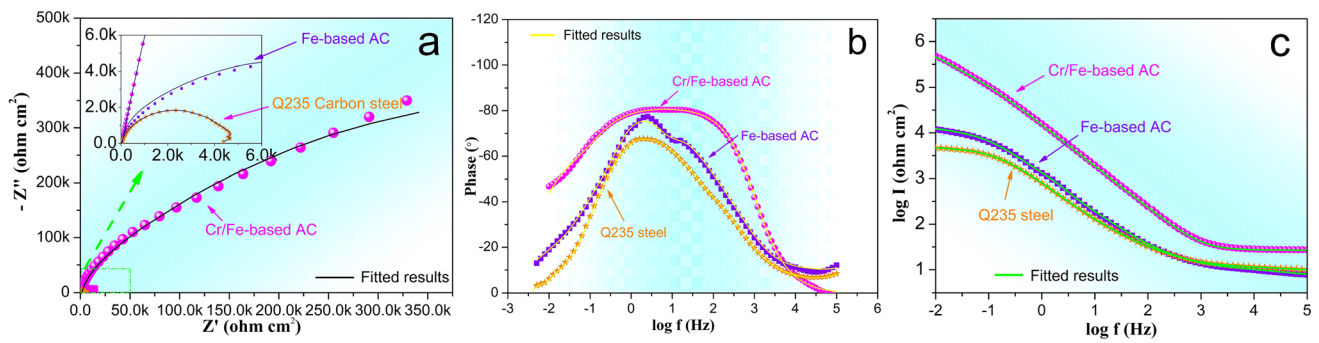


Fig. 7 Equivalent circuit simulation diagram; (a) Q235 carbon steel, (b) Fe-based AC, (c) Cr/Fe-based AC

Table 3 Electrochemical parameters obtained from electrochemical impedance spectroscopy (EIS)

Samples	OCP, mV	$R_s$ , $\Omega \text{ cm}^2$	$R_p$ , $\Omega \text{ cm}^2$	$CPE_{p_0}$ , $\Omega^{-1} \text{ cm}^{-2} \text{ s}^{-n}$	$C_c$ , $\Omega^{-1} \text{ cm}^{-2} \text{ s}^{-n}$	$R$ , $\Omega \text{ cm}^2$
Q235 steel	-392.1	11.55	...	0.77	...	$5.1 \times 10^3$
Fe-based AC	-259.6	1.755	12.32	$1.4 \times 10^{-4}$	...	$1.9 \times 10^4 (R_c)$
Cr/Fe-based AC	-197.4	27.64	$2.9 \times 10^5$	$1.2 \times 10^{-5}$	$1.3 \times 10^{-5}$	$6.8 \times 10^5 (R_f)$

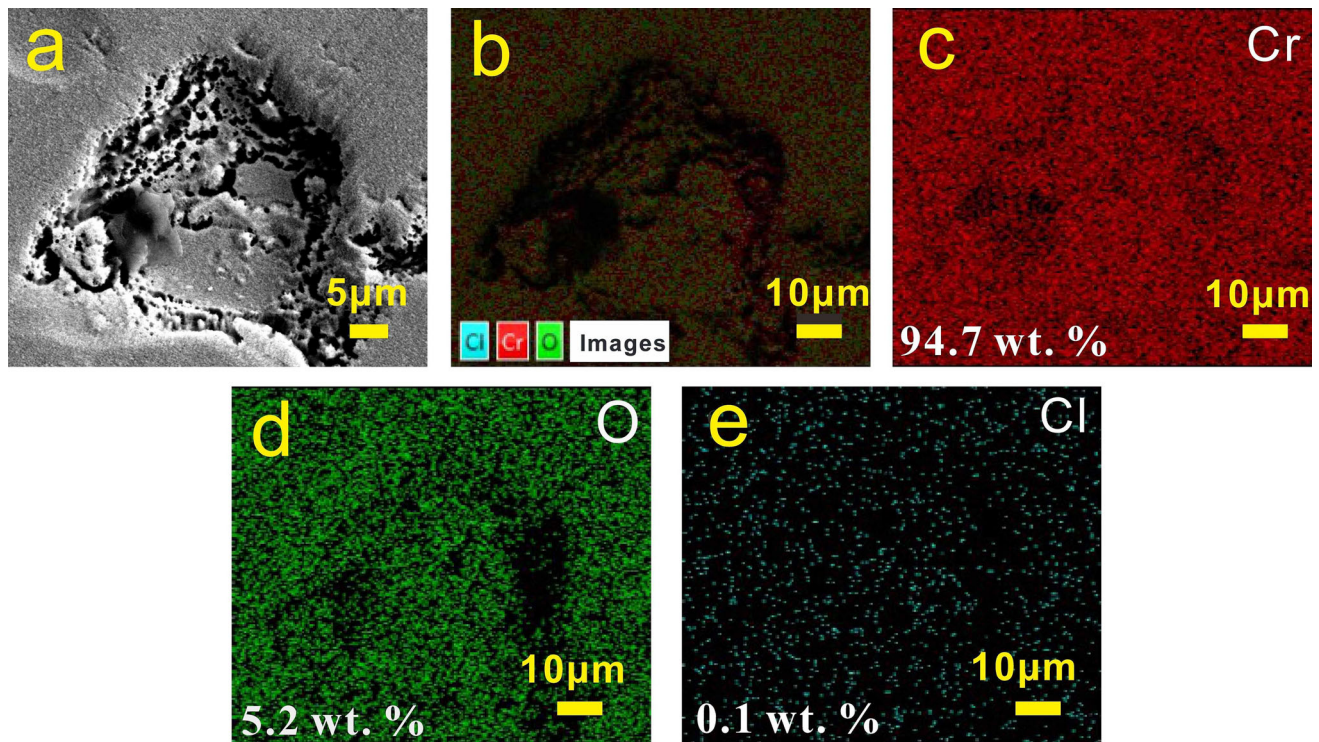


Fig. 8 (a) Surface morphology after corrosion of Cr film/Fe-based amorphous coating, (b) morphology of corrosion pit, (c-e) surface scanning of corrosion pit

formed on the surface of the coating, and these passivated films dissolve on the electrode. This passivated film continues to repeat the process of forming–dissolving–forming until the coating is completely corroded (Ref 28, 29). In this case, the corrosion in the NaCl solution is essentially due to the competition between the formation of the passivated film on the coating surface and the corrosion and dissolution of the coating by  $\text{Cl}^-$ . However, in practice, Fe-based ACs are not

uniform and have an interface between the layers and defects, such as pores. These defects are prone to galvanic corrosion, which significantly affects the corrosion resistance of the coating. Particularly, pores on the surface layer provide channels for  $\text{Cl}^-$  to penetrate the coating after galvanic corrosion, thereby accelerating the corrosion of  $\text{Cl}^-$ . By depositing a Cr film on the surface of the Fe-based AC to achieve sealing, the thickness of the chrome passivation film in

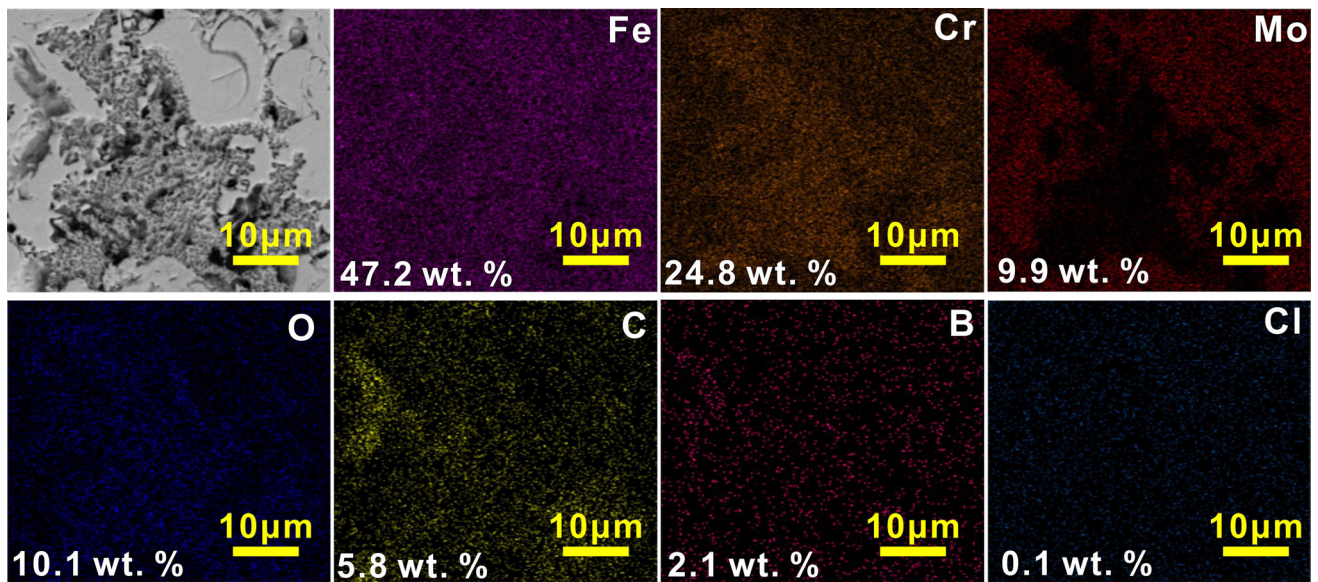


Fig. 9 Corrosion morphology and composition distribution analysis of ferrous amorphous coating surface by EDS scanning

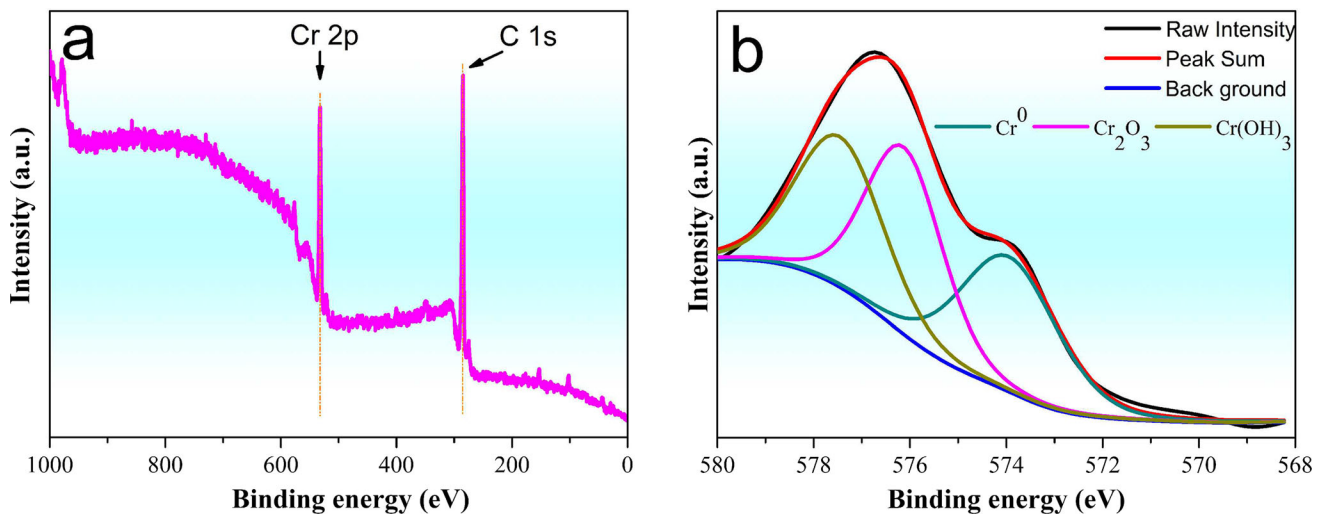


Fig. 10 The fitted XPS spectra for Cr/Fe-based AC in 3.5 wt.% NaCl solution: (a) Cr spectra, (b) Cr 2p spectra

the defect area can be increased, and the penetration of  $\text{Cl}^-$  into the coating through the pores can be avoided. Osozawa (Ref 30) and Keddad (Ref 31) studied the influence of Cr content on the electrochemical corrosion of materials and found that Cr content can improve corrosion resistance and affect electrochemical parameters, such as initial passivation potential.

To further explore the corrosion resistance of Cr/Fe-based AC in a 3.5% NaCl solution, the valence states of the elements in the passivated film formed in the corrosion medium were analyzed by XPS for the Cr/Fe-based AC after corrosion. Figure 10 shows the fitting results of the XPS peaks for the electrochemical corrosion of Cr/Fe-based AC. After electrochemical corrosion, the Cr spectrum consisted of  $2p^{3/2}$  peaks for the Cr and  $\text{Cr}^{3+}$  states. As shown in Fig. 10(b), the peaks at 573.9, 576.1, and 577.4 eV correspond to the  $\text{Cr}^0$ ,  $\text{Cr}^{3+}(\text{Cr}_2\text{O}_3)$ , and  $\text{Cr}^{3+}(\text{Cr}(\text{OH})_3)$  states, respectively. Compared to the spectral intensity of Cr, the spectral intensity of the  $\text{Cr}^{3+}$  state was enhanced, indicating that the Cr atoms on the film surface

were oxidized during immersion in the NaCl solution. Table 3 summarizes the changes in the binding energy positions and peak areas of Cr during the electrochemical testing of the Cr/Fe-based AC. The increase in binding energy reflects the enhanced binding force between the nucleus and electrons (Ref 32). Rodriguez et al. (Ref 33) also showed that changes in the chemical environment can cause the transfer of binding energy. The bonding force between the Cr atoms and electrons on the surface of the Cr/Fe-based AC is affected to a certain extent by the changes in the surrounding chemical environment. Therefore, compared with the binding energy in the standard spectrum, the shift in the binding energy of the Cr atoms is caused by the enhanced oxidation of the film surface. Because the  $\text{Cr}^{3+}$  compound is complex, the  $\text{Cr}^{3+}$  spectrum was fitted with a single peak, and the increase in the binding energy of the  $\text{Cr}^{3+}$  state was mainly due to the formation of  $\text{Cr}_2\text{O}_3$  and  $\text{Cr}(\text{OH})_3$  in the NaCl solution (Table 4).



**Table 4** Variation of Cr binding energy and peak area of Cr/Fe-based AC

Element	Binding energy Ref (Ref 34)	binding energy present	Peak area
Cr	573.8	573.9	1125.8
Cr <sup>3+</sup> (Cr <sub>2</sub> O <sub>3</sub> )	575.9	576.1	1266.2
(Cr(OH) <sub>3</sub> )	577.1	577.4	1155.6

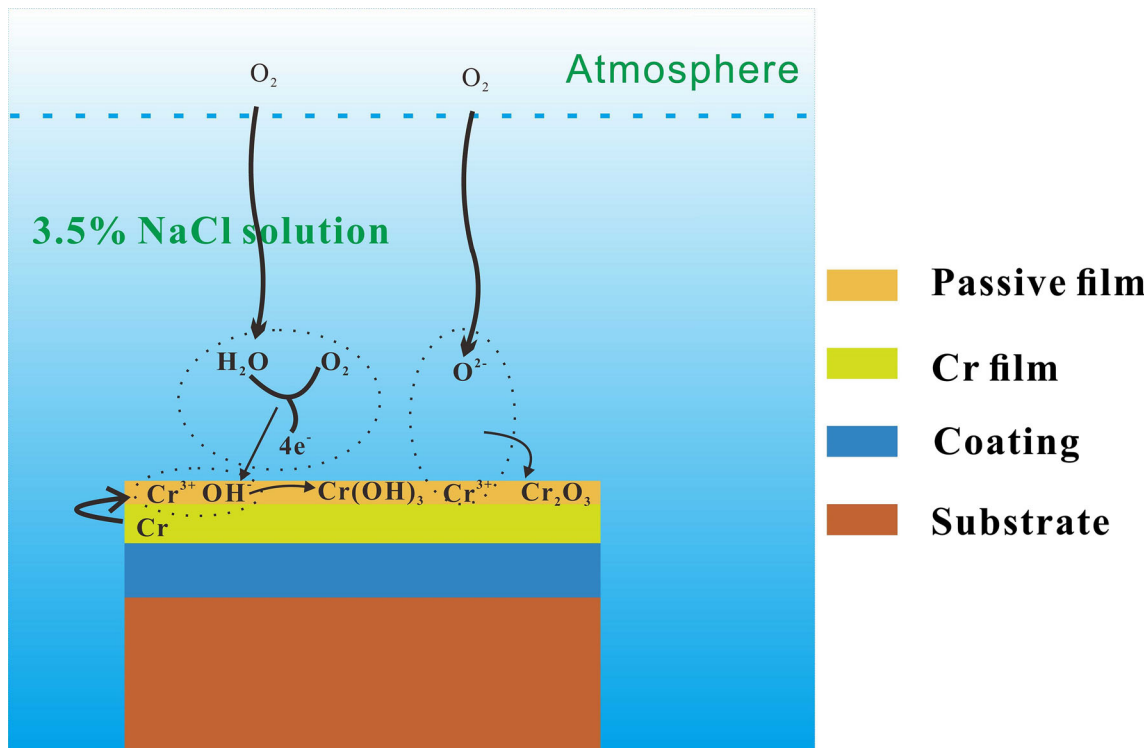
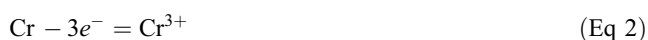
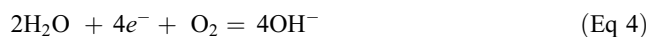


**Fig. 11** Schematic diagram of corrosion mechanism of coating Cr/Fe-based AC

Based on the above XPS analysis (Fig. 10), the formation and evolution of the passivated film during the electrochemical corrosion of the Cr/Fe-based AC can be inferred. First, owing to the oxidation reaction and atomic diffusion on the surface of the Fe-based AC, a primary passivation film of Cr oxide is formed. When immersed in a 3.5% NaCl solution, the oxidation of the film surface is improved, and the activated Cr on the film surface is enhanced. The atoms are further oxidized. In this state, the Cr<sub>2</sub>O<sub>3</sub> and Cr(OH)<sub>3</sub> oxides of Cr are stable, and with the action of the corrosive medium, the Cr atoms are further oxidized and enriched. Finally, a protective passivation film rich in Cr<sup>3+</sup> is formed (Ref 34). Figure 11 shows the corrosion mechanism of Cr/Fe-based AC in 3.5% NaCl solution. In 3.5 wt.% NaCl solution, O<sup>2-</sup>, Cr<sup>3+</sup>, and OH<sup>-</sup> were produced when the electrochemical reaction occurred. Cr<sub>2</sub>O<sub>3</sub> was formed in the passivated film during the process.



The solution product constant ( $K_{sp}$ ) of Cr(OH)<sub>3</sub> is  $6.3 \times 10^{-31}$  (298 K) (Ref 35). OH<sup>-</sup> ions in the solution also react with Cr, which generates a passivated film enriched in Cr(OH)<sub>3</sub>. As the reaction progresses, a uniform and dense passivated film of rich Cr<sub>2</sub>O<sub>3</sub> and Cr(OH)<sub>3</sub> is formed on the Cr/Fe-based AC surface as specified in Reactions (3) and (5), respectively. The passivated film prevents the corrosive medium Cl<sup>-</sup> in the solution from diffusing and penetrating the film and coating, which slows down corrosion.



The polarization curve of the Fe-based AC shows that passivation and re-passivation occurred in 3.5 wt.% NaCl solution. Because the passivated film generated on the surface of the Fe-based AC in the NaCl solution was initially unstable, the passivated film generated on the coating surface was destroyed. With further action of the corrosive medium, the originally passivated film was damaged owing to pitting or dissolution of the passivated film (Ref 36), and the Fe-based AC was re-passivated, forming a stable and dense passivated film. The polarization curve of Cr/Fe-based AC has a larger

**Table 5** The summary of Cr-Fe-based amorphous coatings and other coatings corrosion parameters obtained from Tafel polarization curves

Sample	Prepared technology	$E_{\text{corr}}$ , mV	$J_{\text{corr}}$ , $\mu\text{A cm}^{-2}$	$R$ , $\Omega \text{ cm}^2$	Corrosion rate, mm/year	Ref
Q235 steel	...	- 914	24.56	1821.1	0.28	Present
Fe-based AC	D-gun	- 296	1.73	11,306.8	0.032	Present
Cr/Fe-based AC	D-gun + PVD	- 387	0.165	198,378.7	0.0013	Present
Fe-based AC	HVAF	- 472	5.623	...	...	(Ref 37)
FeCrBSiNbW coating	APS	- 680	4.3	...	...	(Ref 38)
electroplated hard chromium coating	...	- 554	14.12	...	...	(Ref 39)
Fe-based AC	APS	- 530	...	...	...	(Ref 40)
$\text{Fe}_{63}\text{Cr}_8\text{Mo}_{3.5}\text{Ni}_5\text{P}_{10}\text{C}_4\text{B}_4\text{Si}_{2.5}$ amorphous alloys	...	- 260 ± 17	0.504 ± 0.036	...	...	(Ref 41)
$\text{Fe}_{43}\text{Cr}_{16}\text{Mo}_{16}\text{C}_{15}\text{B}_{10}$ amorphous alloy	laser treated	- 554 ± 10	30 ± 5	...	...	(Ref 42)

passivation region (370 mV) in NaCl solution, and the generated passivated film is relatively stable. The results of Tafel extrapolation are listed in Table 5. The polarization resistance ( $1.98 \times 10^5 \Omega \text{ cm}^2$ ) and corrosion rate ( $1.3 \times 10^{-3} \text{ mm/year}$ ) of the Cr/Fe-based AC are better than those of Fe-based AC prepared by other methods, such as APS and HVAF, as shown in Table 5. The above results prove that after PVD, the Cr film is deposited on the surface of the Fe-based AC, sealing the pores on the surface of the coating and further improving the corrosion resistance of the Fe-based AC.

## 4. Conclusions

PVD was used to deposit a Cr film on a detonation-sprayed Fe-based AC to seal the pores, and the corrosion behavior of Fe-based AC and Cr/Fe-based AC in a 3.5% NaCl solution was studied by electrochemical EIS and microstructure analysis. The conclusions are as follows:

- (1) The detonation-sprayed Fe-based AC had an average thickness of  $270 \pm 15 \mu\text{m}$  and a low porosity of approximately 0.8%. The Cr film deposited on the Fe-based AC surface was approximately  $3 \mu\text{m}$ . The XRD analysis further confirmed that only Cr was present in the film, and the EDS results indicated that there were no other elements of impurity in the film.
- (2) Compared with Q235 steel and Fe-based AC, Cr/Fe-based AC showed better corrosion resistance in 3.5% NaCl solution, and the impedance of Cr/Fe-based AC was two orders of magnitude higher than that of Q235 steel; the resistance was one order of magnitude higher than that of Fe-based AC and two orders of magnitude higher than that of Q235 steel. The corrosion rate was one order of magnitude lower than that of Fe-based AC and two orders of magnitude lower than that of Q235 steel.
- (3) Cr/Fe-based AC produced a passivated film of  $\text{Cr}_2\text{O}_3$  and  $\text{Cr}(\text{OH})_3$  on the surface in 3.5 wt.% NaCl solution, preventing the corrosion medium  $\text{Cl}^-$  from diffusing into the film and slowing down the occurrence of corrosion reactions.

## Acknowledgments

This work was supported by the National Natural Science Foundation of China (51901092, 52075234), the key research and development program in Gansu Province (20YF8GA052), the Natural Science Foundation of Gansu Province (20JR10RA494), the “111” project (D21032), and the Hongliu Distinguished Young Talent Support Program of Lanzhou University of Technology.

## Conflict of interest

The authors declare that they have no known competing financial interests or personal relationships that could have appeared to influence the work reported in this paper.

## References

1. B. Huang, C. Zhanga, G. Zhang and H.L. Liao, Wear and Corrosion Resistant Performance of Thermal-Sprayed Fe-Based Amorphous Coatings: A Review, *Surf. Coat. Technol.*, 2019, **377**, p 124896.
2. P.Y. Pan, W.J. Zhou, Y.F. Zhao, Y.T. Wang and N.Q. Zhang, Hot Corrosion Behavior of An Arc Sprayed Fe-Based Amorphous Coating in a Simulated Biomass-Firing Environment, *Corros. Sci.*, 2022, **194**, p 109938.
3. H.M. Zhai, H.Y. Yuan, W.S. Li, X.J. Zhang, X.S. Li and A.H. Cai, Corrosion Resistance Mechanisms of Detonation Sprayed Fe-based Amorphous Coating on AZ31B Magnesium Alloy, *J. Non-Cryst. Solids*, 2022, **576**, p 121276.
4. G.Y. Koga, R. Schulz, S. Savoie, A.R.C. Nascimento, Y. Drolet, C. Bolfarini, C.S. Kiminami and W.J. Botta, Microstructure and Wear Behavior of Fe-Based Amorphous HVOF Coatings Produced from Commercial Precursors, *Surf. Coat. Technol.*, 2017, **309**, p 938–944.
5. Y.J. Sun, R. Yang, L. Xie, W.R. Wang, Y.B. Li, S.L. Wang, H.X. Li, J.M. Zhang and J.S. Zhang, Interfacial Bonding Mechanism and Properties of HVOF-Sprayed Fe-Based Amorphous Coatings on LA141 Magnesium Alloy Substrate, *Surf. Coat. Technol.*, 2021, **426**, p 127801.
6. X.Q. Liu, Y.S. Wu, Z.G. Qiu, Z.Y. Lu, S.Q. Yao, S.Y. Zhuo and D.C. Zeng, Simultaneously Enhancing Wear and Corrosion Resistance of HVAF-Sprayed Fe-Based Amorphous Coating from Mo Clad Feedstock, *J. Mater. Process. Tech.*, 2022, **302**, p 117465.
7. E. Sadeghi and S. Joshi, Chlorine-Induced high-Temperature Corrosion and Erosion-Corrosion of HVAF and HVOF-Sprayed Amorphous Fe-Based Coatings, *Surf. Coat. Technol.*, 2019, **371**, p 20–35.
8. G.Z. Ma, S.Y. Chen, P.F. He, H.D. Wang, Y.Y. Zhou, Q. Zhao and G.L. Li, Particle in-Flight Status and Its Influence on the Properties of Supersonic Plasma-Sprayed Fe-Based Amorphous Metallic Coatings, *Surf. Coat. Technol.*, 2019, **358**, p 394–403.
9. H.M. Zhai, X.Q. Li, W.S. Li, B. Cheng, D.Q. He, X.J. Zhang and S. Cui, Strategy for Improving the Wear-Resistance Properties of

- Detonation Sprayed Fe-Based Amorphous Coatings by Cryogenic Cycling Treatment, *Surf. Coat. Technol.*, 2021, **410**, p 126962.
10. X.Q. Li, H.M. Zhai, W.S. Li, S. Cui, W.C. Ning and X.L. Qiu, Dry Sliding Wear Behaviors of Fe-Based Amorphous Metallic Coating Synthesized by D-Gun Spray, *J. Non-Cryst. Solids*, 2020, **537**, p 120018.
  11. L. Xie, X. Xiong, Y. Zeng and Y.M. Wang, The Wear Properties and Mechanism of Detonation Sprayed Iron-Based Amorphous Coating, *Surf. Coat. Technol.*, 2019, **366**, p 146–155.
  12. K. Ramadan and P. Barry Butler, Analysis of Particle Dynamics and Heat Transfer in Detonation Thermal Spraying Systems, *J. Therm. Spray Technol.*, 2004, **13**, p 248–264.
  13. V. Ulianitsky, A. Shtertser, S. Zlobin and I. Smurov, Computer-Controlled Detonation Spraying: From Process Fundamentals Toward Advanced Applications, *J. Therm. Spray Technol.*, 2011, **20**, p 791–801.
  14. H.M. Zhai, M.J. Ou, S. Cui, W.S. Li, X.J. Zhang, B. Cheng, D.Q. He, X.S. Li and A.H. Cai, Characterizations of the Deposition Behavior and Mechanical Properties of Detonation Sprayed Fe-Based Amorphous Coatings, *J. Mater. Res. Technol.*, 2022, **18**, p 2506–2518.
  15. V. Ulianitsky, A. Shtertser, S. Zlobin and I. Smurov, Computer-Controlled Detonation Spraying: From Process Fundamentals Toward Advanced Applications, *J. Therm. Spray Technol.*, 2011, **20**, p 791–801.
  16. Z. Zhou, L. Wang, D.Y. He, F.C. Wang and Y.B. Liu, Microstructure and Electrochemical Behavior of Fe-Based Amorphous Metallic Coatings Fabricated by Atmospheric Plasma Spraying, *J. Therm. Spray Technol.*, 2010, **20**, p 344–350.
  17. Y. Wang, Z.Z. Xing, Q. Luo, A. Rahman, J. Jiao, S.J. Qu, Y.G. Zheng and J. Shen, Corrosion and Erosion-Corrosion Behaviour of Activated Combustion high-Velocity Air Fuel Sprayed Fe-based Amorphous Coatings in Chloride-Containing Solutions, *Corros. Sci.*, 2015, **98**, p 339–353.
  18. Y. Wang, Y.G. Zheng, W. Ke, W.H. Sun, W.L. Hou, X.C. Chang and J.Q. Wang, Slurry Erosion-Corrosion Behaviour of High-Velocity Oxygen-Fuel (HVOF) Sprayed Fe-Based Amorphous Metallic Coatings for Marine Pump in Sand-Containing NaCl Solutions, *Corros. Sci.*, 2011, **53**, p 3177–3185.
  19. J. Jiao, Q. Luo, X.S. Wei, Y. Wang and J. Shen, Influence of Sealing Treatment on the Corrosion Resistance of Fe-Based Amorphous Coatings in HCl Solution, *J. Alloys Compd.*, 2017, **714**, p 356–362.
  20. G.Y. Wang, Z.H. Zhou, X. Zhang, K.C. Zhang, L.T. Wu and G.H. Yang, Synthesis of Novel Waterborne Silicone Modified Acrylic Sealant and its Corrosion Resistance in Fe-Based Amorphous Coatings, *Prog. Org. Coat.*, 2022, **170**, p 106950.
  21. P.J. Tang, D.Q. He, W.S. Li, L.L. Shang, H.M. Zhai, L.P. Wang and G.A. Zhang, Achieving Superior Hot Corrosion Resistance by PVD/HVOF Duplex Design, *Corros. Sci.*, 2020, **175**, p 108845.
  22. W.S. Li, Y.T. Zhao, D.Q. He, Q. Song, X.W. Sun, S.C. Wang, H.M. Zhai, W.W. Zheng and R.J.K. Wood, Optimizing Mechanical and Tribological Properties of DLC/Cr<sub>3</sub>C<sub>2</sub>-NiCr Duplex Coating Via Tailoring Interlayer Thickness, *Surf. Coat. Technol.*, 2022, **434**, p 128198.
  23. K.A. Najjar, N.A. Sheikh and M.M. Butt, Enhancing the Wear Resistance of WC-Co Cutting Inserts Using Synthetic Diamond Coatings, *Ind. Lubr. Tribol.*, 2018, **70**, p 1224–1233.
  24. K.A. Najjar, N.A. Sheikh, M.M. Butt, S. Mushtaq and M.A. Shah, Engineered Synthetic Diamond Coating as a Protective Layer for Tribological and Machining Applications: A Review, *J. Bio. Tribol. Corros.*, 2019, **5**, p 59.
  25. Y. Yang, C. Zhang, Y. Peng, Y. Yu and L. Liu, Effects of Crystallization on the Corrosion Resistance of Fe-Based Amorphous Coatings, *Corros. Sci.*, 2012, **59**, p 10–19.
  26. M.M. Liu, H.X. Hua, Y.G. Zheng, J.Q. Wang, Z.H. Gan and S. Qiu, Effect of Sol-Gel Sealing Treatment Loaded with Different Cerium Salts on the Corrosion Resistance of Fe-Based Amorphous Coating, *Surf. Coat. Technol.*, 2019, **367**, p 311–326.
  27. L.M. Zhang, M.C. Yan, S.D. Zhang, L.Y. Zhu, A.J. Umoh, A.L. Ma, Y.G. Zheng and J.Q. Wang, Significantly Enhanced Resistance to SRB Corrosion Via Fe-Based Amorphous Coating Designed with High Dose Corrosion-Resistant and Antibacterial Elements, *Corros. Sci.*, 2020, **164**, p 108305.
  28. R.Q. Guo, C. Zhang, Q. Chen, Y. Yang, N. Li and L. Liu, Study of Structure and Corrosion Resistance of Fe-Based Amorphous Coatings Prepared by HVOF and HVOF, *Corros. Sci.*, 2011, **53**, p 2351–2356.
  29. T.J. Lin, H.H. She, C.Y. Lee and H.B. Lee, The Study of Mechanical Properties and Corrosion Behavior of the Fe-Based Amorphous Alloy Coatings Using High Velocity Oxygen Fuel Spraying, *J. alloys compd.*, 2021, **867**, p 159132.
  30. K. Osozawa and H.J. Engell, The Anodic Polarization Curves of Iron-Nickel-Chromium Alloys, *Corros. Sci.*, 1966, **6**(8), p 389–393.
  31. M. Keddad, O.R. Mattos and H. Takenouti, Mechanism of Anodic Dissolution of Iron-Chromium Alloys Investigated by Electrode Impedances-I. Experimental Results and Reaction Model, *Electrochim. Acta*, 1986, **31**(9), p 1147–1158.
  32. J.J. Si, X.H. Chen, Y.H. Cai, Y.D. Wu, T. Wang and X.H. Hui, Corrosion Behavior of Cr-Based Bulk Metallic Glasses in Hydrochloric Acid Solutions, *Corros. Sci.*, 2016, **107**, p 123–132.
  33. J.A. Rodriguez and D.W. Goodman, The Nature of the Metal-Metal Bond in Bimetallic Surfaces, *Science*, 1992, **257**(5072), p 897–903.
  34. W.P. Tian, H.W. Yang and S.D. Zhang, Synergistic Effect of Mo W Mn and Cr on the Passivation Behavior of a Fe-Based Amorphous Alloy Coating, *Acta Metall. Sin. (Engl. Lett.)*, 2018, **31**(3), p 308–320.
  35. J.F. Huang, Y.T. Li, J.H. Wu, P.Y. Cao, Y.L. Liu and G.B. Jiang, Floatable, Macroporous Structured Alginate Sphere Supporting Iron Nanoparticles Used for Emergent Cr(VI) Spill Treatment, *Carbohydr. Polym.*, 2016, **146**, p 115–122.
  36. G.T. Burstein, C. Liu and R.M. Souto, Origins of Pitting Corrosion, *Corros. Eng. Sci. Technol.*, 2004, **39**(1), p 25–30.
  37. G. Wang, Z.J. Huang, P. Xiao and X.B. Zhu, Spraying of Fe-Based Amorphous Coating with high Corrosion Resistance by HVOF, *J. Manuf. Process.*, 2016, **22**, p 34–38.
  38. J.B. Cheng, Z.H. Wang and B.S. Xu, Wear and Corrosion Behaviors of FeCrBSiNbW Amorphous/Nanocrystalline Coating Prepared by Arc Spraying Process, *J. Therm. Spray Technol.*, 2012, **21**(5), p 1025–1031.
  39. L. Qiao, Y.P. Wu, S. Hong, Y.J. Qin, W. Shi and G.Y. Li, Corrosion Behavior of HVOF-Sprayed Fe-Based Alloy Coating in Various Solutions, *J. Mater. Eng. Perform.*, 2017, **26**, p 3813–3820.
  40. X.B. Zhao and Z.H. Ye, Microstructure and Corrosion Resistance of Fe-Based Amorphous Coating Prepared Atmospheric Plasma Spraying, *Adv. Mater. Res.*, 2012, **557–559**, p 1768–1771.
  41. J.W. Li, L.J. Yang, H.R. Ma, K.M. Jiang, C.T. Chang, J.Q. Wang, Z.L. Song, X.M. Wang and R.W. Li, Improved Corrosion Resistance of Novel Fe-Based Amorphous Alloys, *Mater. Des.*, 2016, **95**, p 225–230.
  42. M.S. Bakare, K.T. Voisey, K. Chokethawai and D.G. McCartney, Corrosion Behaviour of Crystalline and Amorphous Forms of the Glass Forming Alloy Fe<sub>43</sub>Cr<sub>16</sub>Mo<sub>16</sub>C<sub>15</sub>B<sub>10</sub>, *J. Alloys Compd.*, 2012, **527**, p 210–218.

**Publisher's Note** Springer Nature remains neutral with regard to jurisdictional claims in published maps and institutional affiliations.

Springer Nature or its licensor (e.g. a society or other partner) holds exclusive rights to this article under a publishing agreement with the author(s) or other rightsholder(s); author self-archiving of the accepted manuscript version of this article is solely governed by the terms of such publishing agreement and applicable law.